bioRxiv preprint doi: https://doi.org/10.1101/2020.09.29.319707; this version posted October 1, 2020. The copyright holder for this preprint (which was not certified by peer review) is the author/funder. All rights reserved. No reuse allowed without permission.

Architecture of the Tuberous Sclerosis Protein Complex

Kailash Ramlaul[1]*, Wencheng Fu[2]*, Hua Li[2]*, Natàlia de Martin Garrido[1], Lin He[3], Wei Cui[4], Christopher H S Aylett[1]†, & Geng Wu[2]†

[1] Section for Structural Biology, Department of Medicine, Imperial College London, Exhibition Road, London, SW7 2BB, United Kingdom

[2] State Key Laboratory of Microbial Metabolism, School of Life Sciences & Biotechnology, The Joint International Research Laboratory of Metabolic & Developmental Sciences MOE, Shanghai Jiao Tong University, Shanghai, China

[3] Instrumental Analysis Center, Shanghai Jiao Tong University, Shanghai, China

[4] Institute of Reproductive and Developmental Biology, Faculty of Medicine, Imperial College London, Du Cane Road, London, W12 0NN, United Kingdom

* These authors contributed equally to this study.

† To whom correspondence may be addressed:

C.H.S.A. - c.aylett@imperial.ac.uk

G.W. - geng.wu@sjtu.edu.cn

bioRxiv preprint doi: https://doi.org/10.1101/2020.09.29.319707; this version posted October 1, 2020. The copyright holder for this preprint (which was not certified by peer review) is the author/funder. All rights reserved. No reuse allowed without permission.

Abstract

The Tuberous Sclerosis Complex (TSC) protein complex (TSCC), comprising of three subunits TSC1, TSC2, and TBC1D7, is widely recognised as a key integration hub for cell growth and intracellular stress signals upstream of the mammalian target of rapamycin complex 1 (mTORC1). The TSCC negatively regulates mTORC1 by acting as a GTPase-activating protein (GAP) towards the small GTPase Rheb. Both human TSC1 and TSC2 are important tumor suppressors, and their mutations underlie the tuberous sclerosis disease.

We used single-particle cryo-EM to reveal the organisation and architecture of the complete human TSCC. We show that TSCC forms an elongated scorpion-like structure, consisting of a "body" in the middle, and a "pincer" and a "tail" at each side. The "body" is composed of a flexible TSC2 HEAT repeat dimer, along the inner surface of which runs the TSC1 coiled-coil backbone, breaking the symmetry of the dimer. Each end of the body is structurally distinct, representing the N- and C-termini of TSC1; a "pincer" is formed by the highly flexible N-terminal TSC1 core domains and a barbed "tail" makes up the TSC1 coiled-coil-TBC1D7 junction. The TSC2 GAP domain is found abutting the centre of the body on each side of the dimerisation interface, poised to bind a pair of Rheb molecules at a similar separation to the pair in activated mTORC1.

Our architectural dissection reveals the mode of association and topology of the complex, casts light on the recruitment of Rheb to the TSCC, and also hints at functional higher order oligomerisation, which has previously been predicted to be important for Rheb-signalling suppression.

bioRxiv preprint doi: https://doi.org/10.1101/2020.09.29.319707; this version posted October 1, 2020. The copyright holder for this preprint (which was not certified by peer review) is the author/funder. All rights reserved. No reuse allowed without permission.

Introduction

Tuberous sclerosis complex (TSC) is an autosomal dominant disease characterised by benign tumours in multiple organs (Henske *et al*, 2016). It is caused by mutations in either of the genes *TSC1* or *TSC2*, which encode the 130 kDa TSC1/hamartin and the 200 kDa TSC2/tuberin tumour suppressor proteins respectively. TSC1 contains an N-terminal α-helical 'core' domain and a coiled-coil at the C-terminus which is required for binding TSC2 (Nellist *et al*, 1999; Santiago Lima *et al*, 2014; van Slegtenhorst *et al*, 1998). TSC2 contains a long α-solenoid domain at the N-terminus and a C-terminal GTPase activating protein (GAP) domain, which is the sole catalytically active domain in the complex. Together with a small third subunit TBC1D7 (Dibble *et al*, 2012), TSC1 and TSC2 assemble to form the TSC protein complex (TSCC).

TSCC signalling restricts cell growth by negatively regulating mTORC1, the central coordinator of metabolism (González & Hall, 2017; Ramlaul & Aylett, 2018). Directly upstream of mTORC1, Rheb, a small GTPase localized to lysosomes through C-terminal farnesylation (Clark *et al*, 1997), stimulates mTORC1 kinase activity when GTP-bound (Yang *et al*, 2017). The TSCC stimulates Rheb GTPase activity, accumulating the GTPase in the inactive, GDP-bound, state to suppress mTORC1 (Huang & Manning, 2008). Spatial regulation of TSCC between the cytoplasm and lysosome is known to be pivotal for its function as a Rheb-GAP, with the current understanding being that TSCC translocates to the lysosome surface to catalytically and sterically inhibit mTORC1 by binding to Rheb and sequestering it (Menon *et al*, 2014; Demetriades *et al*, 2016). This translocation is reversed on TSC2 phosphorylation by AKT (Menon *et al*, 2014), and other kinases, which are thought to regulate localisation through an unknown mechanism involving 14-3-3 binding (Shumway *et al*, 2003; Cai *et al*, 2006), as well as TSCC breakdown by ubiquitination-targeted TSC2 degradation (Benvenuto *et al*, 2000; Chong-Kopera *et al*, 2006).

The architecture of the TSCC remains completely unknown, although small fragments of the complex have been structurally characterised. The core domain of *S. pombe* TSC1 (Sun *et al*, 2013), an N-terminal α-solenoid fragment of *C. thermophilum* TSC2 (Zech *et al*, 2016), and most recently the *Ct*TSC2$_{GAP}$ domain (Hansmann *et al*, 2020) have been resolved crystallographically. Furthermore, two co-crystal structures of TBC1D7 interacting with C-terminal coiled-coil fragments of TSC1 have been determined (Gai *et al*, 2016; Qin *et al*, 2016). In this study, we have used cryogenic electron microscopy (cryo-EM) to examine the molecular architecture of the full-length, human holo-TSCC.

bioRxiv preprint doi: https://doi.org/10.1101/2020.09.29.319707; this version posted October 1, 2020. The copyright holder for this preprint (which was not certified by peer review) is the author/funder. All rights reserved. No reuse allowed without permission.

Results

Structure of TSCC

We cloned human TSC1, TSC2, and TBC1D7 for expression in human embryonic kidney cells, and Rheb for expression in *Escherichia coli*. A clone yielding an internal deletion of TSC1(Δ400-600) was used for SEC-MALLS to minimise inter-complex interactions. While both TBC1D7 and TSC1 could be expressed and purified independently, TSC2 could not be produced in the absence of TSC1, being degraded in cell (Supp. Fig. 1), consistent with the role of TSC1 in preventing TSC2 degradation (Benvenuto *et al*, 2000; Chong-Kopera *et al*, 2006).

We retrieved the complete human TSCC from cell lysate using FLAG-tagging, and purified the TSCC from most remaining contaminants by size-exclusion chromatography (SEC) (Fig. 1A). Purified TSCC exhibited its physiological GAP activity towards Rheb (Fig. 1B). SEC of the full-length TSCC yielded a broad peak with an estimated mass of 5,200 kDa, due to inter-TSCC lateral interactions (Supp. Fig. 2), whereas SEC at lower concentrations, or TSC1(Δ400-600) TSCC, yielded a defined peak with an estimated molecular weight by multi-angle LASER light scattering of 690-710 kDa (Fig. 1C), roughly corresponding to a composition of 2:2:2-TSC1:TSC2:TBC1D7.

We initially investigated the molecular architecture of the TSCC by negative staining. We observed extremely flexible, independent particles, however three defined ordered regions could be isolated, and two-dimensional averaging of these regions provided a complete picture (Fig. 1D). The TSCC was extraordinarily elongated (~400 Å) and exhibited a characteristic "scorpion" shape, with a bulkier central "body", flexible "pincer"-like appendage at one end, and a barbed "tail" at the other. Cryo-EM of TSCC at low concentrations revealed identical particles (Fig. 1E), whereas at higher concentrations we observed web-like networks which appear to be formed of head-to-tail TSCC particles (Supp. Fig. 2). Once again, complete TSCC particles were too flexible to average beyond low resolution (Fig. 2A). We isolated the same regions; both the "pincer" and "tail" proved to be strongly preferentially oriented and flexible, the "pincer" refining only to low resolution (11 Å), and the "tail" to low-intermediate resolution (9 Å) (Fig. 2A). The body of the TSCC exhibited pseudo-C2 symmetry, and was refined in C2 initially to 4.2 Å, before symmetry was relaxed for a final C1 structure at 4.5 Å (Fig 2A).

The resolution of the "body" was high enough to trace chains and identify all secondary structural elements, but too low to definitively assign sequence. The published structure of the TSC2 GAP domain (Hansmann *et al*, 2020) fitted unambiguously into density adjoining a central α-solenoid on each side of the origin of C2 pseudo-symmetry (Fig. 2A, Supp. Fig. 3). At the juncture of the two α-solenoids, we observed a dimerisation interface comprising two back-to-back β-sheets (Fig. 2A). With the exception of the GAP domain, the only β-elements remaining predicted within the sequence

bioRxiv preprint doi: https://doi.org/10.1101/2020.09.29.319707; this version posted October 1, 2020. The copyright holder for this preprint (which was not certified by peer review) is the author/funder. All rights reserved. No reuse allowed without permission.

of any TSC protein are at the C-terminus of the α-solenoid of TSC2 (Supp. Fig. 3), which is consistent with the TSC2 α-solenoids running outwards from C-terminus to N-terminus from the dimerisation site. Because of the extensive regions of predicted unstructured sequence within this region, it is entirely possible that there are multiple topologies for the dimerisation interface and the two TSC2 molecules cannot be clearly delineated. The C2 symmetry of TSC2 is broken by two helices running directly across the top of the dimerisation site. This helical density forms a weakly connected "backbone" running over both GAP domains, and along the TSC2 α-solenoid outwards to both the "pincer" and "tail". We assign this continuous helical coiled-coil as that from the C-terminal regions of TSC1, implying that the two ends are its N- and C-terminus respectively. The "pincer" density is uninterpretable, however the TSC1-TBC1D7 structure (Qin *et al*, 2016) unambiguously fits the density corresponding to the "barb" lying on the α-solenoid of the "tail" (Fig. 2A, Supp. Fig. 4), confirming the orientation of the TSC1 dimer, and implying that the "pincer" is made up of the TSC1 HEAT-domains.

Under the reasonable assumption that the GAP-Rheb interaction will mirror that of the published Rap-GAP complex (Scrima *et al*, 2008), we have docked Rheb accordingly. The natural docking yields no clashes with the current structure, and implies a further interaction with the two helices adjoining the GAP domain (Fig. 2B). We note that the Rheb farnesylation sites would both be situated on the same side of the TSCC, consistent with this being the correct orientation for lysosomal binding.

Tumorigenic mutations in TSC2

TSC2 is an important tumor suppressor protein, mutations of whose encoding gene are highly correlated with tuberous sclerosis. We examined the tumorigeic missense mutations of TSC2 (Table 1) frequently listed in the Tuberous sclerosis database (http://chromium.lovd.nl/LOVD2/TSC/home.php?select_db=TSC2). Half of these TSC2 residues with tumorigeic missense mutations (27 of 54 residues total) occur on the N-terminal α-solenoid domain, most of which clustering together (such as residues A84, P91, and E92; residues C244, M286, G294, E337, A357, and R367; residues G440, L448, A460, R462, L466, and L493; residues A583, H597, Y598, A607, R611, R622, and M649; residues L826, L847, R905, and L916; Suppl. Fig. 3A). Given that the N-terminal domain (NTD) of TSC2 is found to closely contact the GAP domain of TSC2 (Fig. 2), these mutation-clustered regions might represent the GAP-contacting sites on TSC2-NTD. In *tsc2* mutant cancer cells harbouring these TSC2 missense mutations, the association between TSC2-NTD and TSC2-GAP might be disrupted, leading to diminished GAP activity toward Rheb and abnormally elevated mTORC1 activity.

bioRxiv preprint doi: https://doi.org/10.1101/2020.09.29.319707; this version posted October 1, 2020. The copyright holder for this preprint (which was not certified by peer review) is the author/funder. All rights reserved. No reuse allowed without permission.

In addition, the C-terminal GAP domain of TSC2 represents the region possessing the second highest number of tumorigeic missense-mutated amino acids, with more than 30% of all residues listed (17 of 54 in Table 1). A lot of these disease-related residues are highly conserved across a vast variety of organisms from human to yeast, such as H1620, G1642, N1643, and R1743 (Suppl. Fig. 3A). Presumably, these residues play key roles for TSC2-GAP's enzymatic activity. Interestingly, H1620, G1642, and N1643 on TSC2-GAP correspond to H266, G289, and N290 of RapGAP, which directly contact or are very close to Rap in the Rap-RapGAP crystal structure (Scrima et al., 2008, Supp. Fig. 5). These residues might be responsible for interaction with Rheb, and their mutations in tuberous sclerosis patients could subvert the GAP activity of TSC2.

bioRxiv preprint doi: https://doi.org/10.1101/2020.09.29.319707; this version posted October 1, 2020. The copyright holder for this preprint (which was not certified by peer review) is the author/funder. All rights reserved. No reuse allowed without permission.

Discussion

We show that the TSCC forms an elongated, flexible architecture, comprising two copies of each of TSC1, TSC2, and TBC1D7. The orientation of Rheb implied by the GAP domains (Fig. 2B) matches the slight curvature of the complex, and the lysosomal membrane will therefore lie on the opposite side of the TSCC from the TSC1 backbone. The super-structure observed forming at higher concentrations (Supp. Fig. 2) may well play a part in retaining TSCC at the lysosome and reducing the off-rate once Rheb signalling has been suppressed as previously predicted (Menon *et al*, 2014). Further structural investigation of these inter-TSCC interactions, likely mediated by the TSC1 termini (Nellist *et al*, 1999; Hoogeveen-Westerveld *et al*, 2010), is required to understand the higher-order organisation of TSCC and its role in mTORC1 regulation.

The C2 symmetry of each of the dimeric TSC proteins is broken by the presence of the other, that of TSC1 by the curvature of its coiled-coil along the TSC2 α-solenoids, and that of TSC2 by the involvement of TSC1 in its dimerisation. We have confirmed once again that while TSC1 can fold independently of TSC2, the reverse does not occur (Benvenuto *et al*, 2000; Chong-Kopera *et al*, 2006; Woodford *et al*, 2017). Our architecture suggests a structural explanation for this observation, and indicating direct TSC1 involvement in the TSC2 dimerisation interface. The previously observed breakdown of TSC2, following ubiquitination in the absence of TSC1 (Benvenuto *et al*, 2000; Chong-Kopera *et al*, 2006), would be expected when structural elements cannot fold appropriately in the absence of their partner. This would also constrain the presence of functional TSC2 to subcellular regions containing TSC1 dimers.

In complete agreement with the conclusions of the Manning group (Menon *et al*, 2014), the presence of the TSCC will both catalytically and sterically prevent Rheb–mTORC1 interactions (Fig. 2B), rotating the Rheb pair in relation to its position when interacting with mTORC1. We believe that one of the most interesting observations from our results is that TSC2 binds Rheb as such a pair, as does mTORC1. Despite the fact that they are completely different in architecture and approach from different directions, the TSCC GAP domains are poised to bind two copies of Rheb at an almost identical separation to that resolved for Rheb in the structure of activated mTORC1 (Fig. 2B). While it is possible that this is entirely happenstance, this would also be expected were Rheb bound by each partner as part of a greater, at least dimeric, complex on the lysosomal surface.

Our improved architectural understanding of the TSCC provides a starting point for the investigation of the molecular mechanisms by which TSCC directly regulates Rheb, and poses new questions on the nature of the superstructures formed by TSCC complexes, their partners, and the involvement of such quaternary structures in mTORC1 regulation.

bioRxiv preprint doi: https://doi.org/10.1101/2020.09.29.319707; this version posted October 1, 2020. The copyright holder for this preprint (which was not certified by peer review) is the author/funder. All rights reserved. No reuse allowed without permission.

Materials and methods

Protein expression and purification

pRK7 plasmids subcloned with FLAG-tagged full-length (FL) human TSC1 (1164 amino acids, UniProtKB/Swiss-Prot accession number Q92574-1) and FLAG-tagged FL human TSC2 (1807 amino acids, UniProtKB/Swiss-Prot accession number P49815-1) were purchased from Addgene, and pRK7 was subcloned with FLAG-tagged human TBC1D7 (293 amino acids, GenBank accession number AAH07054). FL TSC1-TSC2-TBC1D7 ($TSCC_{FL}$) plasmids, or $TSC1_{\Delta 400\text{-}600}$-TSC2-TBC1D7 ($TSCC_{1\Delta}$) plasmids, were co-transfected into human embryonic kidney (HEK) Expi293F cells (Thermo Fisher Scientific, Waltham, MA, USA). Two days after transfection, the harvested Expi293F cells were lysed by three cycles of freeze-thaw in lysis buffer (20 mM Tris, pH 8.0, 300 mM NaCl, 2 mM TCEP, 0.5 mM PMSF, 1 μg/ml aprotinin, and 1 μg/ml leupeptin), and TSCC was purified from the cell lysate by M2 anti-FLAG affinity chromatography (Sigma) followed by size exclusion chromatography using a Superose 6 column (GE Healthcare) pre-equilibrated with buffer containing 20 mM Tris, pH 8.0, 300 mM NaCl, and 2 mM TCEP. The identity of each TSCC component was verified by ESI-MS (Mass Spectrometry Facility, University of St. Andrews).

The cDNA of residues 1-169 of human Rheb (184 amino acid isoform, GenBank accession number EAW53989) was subcloned into the pET28a vector (Novagen), with an N-terminal 6×His-tag. Rheb was overexpressed in *E.coli* strain BL21(DE3). After lysis of the bacteria with a cell homogenizer (JNBIO) and clarification, the lysate was subjected to Ni^{2+}-NTA affinity chromatography (Qiagen) followed by size exclusion chromatography using a Superdex 200 column (GE Healthcare) pre-equilibrated with buffer containing 20 mM Tris, pH 8.0, 200 mM NaCl, and 2 mM DTT.

GTPase activity endpoint assay

The GTPase activity of Rheb was assayed using the QuantiChrom ATPase/GTPase assay kit (BioAssay Systems), in which the amount of released inorganic phosphate was measured through a chromogenic reaction with malachite green. In the assays 75 nM RheB, either alone or mixed with 227.5 nM $TSCC_{FL}$, were added to the reaction buffer (40 mM Tris, pH 8.0, 80 mM NaCl, 8 mM MgOAc, 1 mM EDTA and 14 mM GTP) at 28 °C for 40 min. A further 200 μL of assay kit reagent was then added, and the reaction was incubated for 20 min, before a microplate reading at OD 620 nm was measured. Spontaneous GTP hydrolysis was calculated by measuring background absorbance in the absence of Rheb and sample values were normalised by subtraction of the background. Each experiment was repeated three times.

bioRxiv preprint doi: https://doi.org/10.1101/2020.09.29.319707; this version posted October 1, 2020. The copyright holder for this preprint (which was not certified by peer review) is the author/funder. All rights reserved. No reuse allowed without permission.

Size exclusion chromatography–multi-angle laser light scattering (SEC-MALLS)

Both full length TSCC and $TSCC_{1\Delta}$ (consisting of TSC1 deleting residues 400-600, TSC2, and TBC1D7) were analysed by SEC-MALLS using an Infinity liquid chromatography system (Agilent Technologies), linked to a Dawn Heleos multi-angle light scattering detector (Wyatt Technology) and Optilab T-rEX refractive index detector (Wyatt Technology). The sample was injected onto a Superose 6 10/300 size exclusion column (GE Healthcare) pre-equilibrated overnight with buffer containing 25 mM K-HEPES, pH 7.6, 250 mM KCl, 0.5 mM EDTA, 1 mM TCEP and trace amounts of NaN_3, using 0.2 mL/min flow rate at room temperature. In-line UV absorbance, light scattering and refractive index measurements were analysed using the ASTRA software package (Wyatt Technology) to determine molar mass estimates.

Sample preparation for cryo-EM studies

TSCC, after the above purification steps, was loaded onto a Superose 6 10/300 size exclusion chromatography column (GE Healthcare) pre-equilibrated with a preparation buffer containing 25 mM K-HEPES, pH 7.6, 175 mM KCl or 150 mM LiCl, 1 mM TCEP, and 0.5 µM EDTA. TSCC eluted as a single peak with a slight shoulder at lower retention volume. The integrity of the complex was confirmed by SDS-PAGE of both the peak and shoulder fractions. Main peak fractions were combined and concentrated to 0.1–0.2 mg/mL using Amicon 100 kDa molecular weight cut-off (MWCO) centrifugal filters and used for grid preparation.

Generation of an initial TSCC reference density

A sample of concentrated wild-type $TSCC_{FL}$ was applied to a carbon-coated holey carbon grid (R1.2/1.3, Quantifoil) and stained with 2% (w/v) uranyl acetate. A total of 224 micrographs were collected using an FEI Tecnai T12 electron microscope (Thermo Fisher Scientific, Waltham, MA, USA) at a magnification of 81,000-fold, an acceleration voltage of 120 kV, and a total dose of 50 $e^-/Å^2$ over a defocus range of -0.5 to -2.0 µm. A dataset of 9 597 particles was selected manually using BOXER. The parameters of the contrast transfer function were determined using CTFFIND4. Particles were 2D-classified into 100 classes in two dimensions using RELION and sixteen well-defined classes were selected for initial three-dimensional reconstruction. Initial models were created using the initial model functions in EMAN2, refined in three dimensions at low resolution using SPIDER, then filtered to 60 Å and used as an initial reference for automatic refinement in RELION. The resulting initial model at a resolution of 26 Å, with independent volume Fourier Shell Correlation (FSC) of 0.143, was used for further refinement.

bioRxiv preprint doi: https://doi.org/10.1101/2020.09.29.319707; this version posted October 1, 2020. The copyright holder for this preprint (which was not certified by peer review) is the author/funder. All rights reserved. No reuse allowed without permission.

TSCC cryo-EM sample preparation

Samples of concentrated $TSCC_{FL}$ were adsorbed to a thin film of graphene oxide deposited upon the surface of holey carbon copper grids (R2/1, 300 mesh, Quantifoil). Grids were blotted for 2-3 seconds before plunge freezing in liquid ethane using a Vitrobot Mark IV (Thermo Fisher Scientific, Waltham, MA, USA) at 4 ºC and 100% humidity.

TSCC cryo-EM data collection

Data were collected for TSCC on a Titan Krios (Thermo Fisher Scientific, Waltham, MA, USA) at the Electron Bioimaging Centre (eBIC, Diamond Light Source), equipped with a K2 Summit direct electron detector (GATAN, San Diego, USA) and operated at 300 kV, 37000-fold magnification and with an applied defocus range of -0.75 to -3.25 µm. Frames were recorded automatically using EPU, resulting in 5387 images of 3838 by 3710 pixels with a pixel size of 1.35 Å on the object scale. Images were recorded in two successive datasets (of 1880 and 3507 images, respectively) as either 40 or 60 separate frames in electron counting mode, comprising a total exposure of 52.3 or 80.2 $e^{-}Å^{-2}$, respectively.

TSCC cryo-EM data processing

Frames were aligned, summed and weighted by dose according to the method of Grant and Grigorieff using MotionCor2 (Zheng *et al*, 2017) to obtain a final image. Poor-quality micrographs were rejected based on diminished estimated maximum resolution on CTF estimation using CTFFIND4 (Rohou & Grigorieff, 2015) and visually based on irregularity of the observed Thon rings. Particles were selected using BATCHBOXER (Tang *et al*, 2007), and refinement thereafter performed using RELION3 (Scheres, 2012; Zivanov *et al*, 2018).

Two-dimensional reference-free alignment was performed on ~1,500,000 initially boxed particles to exclude those that did not yield high-resolution class averages and to identify the principal ordered regions of the TSCC molecule. Of these, ~300,000 showed resolution extending to high-resolution and were retained for further refinement.

TSCC proved to be highly preferentially oriented on the grid, however it was possible to identify 2D classes for each of the “body”, “pincer” and “tail” regions. Iterated re-centring, two-dimensional refinement, and re-boxing using the neural network particle picker Topaz (Bepler *et al*,

bioRxiv preprint doi: https://doi.org/10.1101/2020.09.29.319707; this version posted October 1, 2020. The copyright holder for this preprint (which was not certified by peer review) is the author/funder. All rights reserved. No reuse allowed without permission.

2018) was performed from the "body" region outwards in order to maximise recovery of the "pincer" and "tail" views and provide a complete description and definitive topology for all three regions.

Particles belonging to the "body" frequently displayed C2 symmetry in 2D class averages, and this particle subset was refined in three dimensions using this symmetry restraint. After several iterations of re-picking particles using Topaz (Bepler *et al*, 2018) and refinement, the final gold-standard refinement of the "body", including 59 524 particles, reached 4.2 Å at an independent FSC = 0.143. The symmetry was subsequently relaxed to C1 and refined (gold-standard) to 4.6 Å resolution at an independent FSC = 0.143. Reconstructions were also performed for the "pincer" and "tail" regions, however these suffered from persistent highly preferred orientation and conformational flexibility, with gold-standard refinements reaching 11 Å and 9 Å resolution, respectively, at an independent FSC = 0.143.

bioRxiv preprint doi: https://doi.org/10.1101/2020.09.29.319707; this version posted October 1, 2020. The copyright holder for this preprint (which was not certified by peer review) is the author/funder. All rights reserved. No reuse allowed without permission.

Acknowledgements

The authors would like to thank Xinqiu Guo at Instrumental Analysis Centre of Shanghai Jiao Tong University for assistance with electron microscopy experiments. G.W. thanks Dr. Sheng Wang, Dr. Xinqi Gong, Lijun Yan, Hongpeng Wang, and Ailiang He for their contribution. We are indebted to the Imperial Centre for Structural Biology and the UK national electron Bio-imaging Centre at Diamond Light Source (proposal EM14769, funded by the Wellcome Trust, MRC and BBSRC) for access to electron microscopy equipment and in particular to Paul Simpson for technical support. The authors would also like to thank Marc Morgan for help with SEC-MALLS analysis, the St. Andrews Proteomics facility for mass spectrometric protein identification and Nadezhda Aleksandrova for GTPase assay preparation. G.W. is supported by National Natural Science Foundation of China (grant numbers 31670106 and 31872627), Shanghai Jiao Tong University Scientific and Technological Innovation Fund, and the National Key R&D Program of China (YS2020YFA090044). C.H.S.A. is supported by a Sir Henry Dale Fellowship jointly funded by the Wellcome Trust and the Royal Society (206212/Z/17/Z).

Author contributions

G.W. and C.H.S.A. conceived of the project. W.F., K.R., and H.L. purified the protein, performed initial negative staining analysis, and carried out the GAP assay. K.R. and N.M.G. carried out and analysed SEC-MALLS experiments. C.H.S.A., K.R., and W.F. prepared samples and grids for cryo-EM, collected electron micrographs and calculated single-particle reconstructions. All authors were involved in the interpretation of results and the drafting of the manuscript.

Competing financial interests

The authors declare that they have no competing financial interests.

Data and materials availability

The cryo-EM density map corresponding {###} of the *Hs*TSCC complex has been deposited in the EM Databank under accession codes EMD-{####}.

bioRxiv preprint doi: https://doi.org/10.1101/2020.09.29.319707; this version posted October 1, 2020. The copyright holder for this preprint (which was not certified by peer review) is the author/funder. All rights reserved. No reuse allowed without permission.

References

Benvenuto G, Li S, Brown SJ, Braverman R, Vass WC, Cheadle JP, Halley DJ, Sampson JR, Wienecke R & DeClue JE (2000) The tuberous sclerosis-1 (TSC1) gene product hamartin suppresses cell growth and augments the expression of the TSC2 product tuberin by inhibiting its ubiquitination. *Oncogene* **19:** 6306–6316

Bepler T, Morin A, Noble AJ, Brasch J, Shapiro L & Berger B (2018) Positive-unlabeled convolutional neural networks for particle picking in cryo-electron micrographs. *Nat. Methods* **10812:** 245–247

Cai S-L, Tee AR, Short JD, Bergeron JM, Kim J, Shen J, Guo R, Johnson CL, Kiguchi K & Walker CL (2006) Activity of TSC2 is inhibited by AKT-mediated phosphorylation and membrane partitioning. *J Cell Biol* **173:** 279–289

Chong-Kopera H, Inoki K, Li Y, Zhu T, Garcia-Gonzalo FR, Rosa JL & Guan KL (2006) TSC1 stabilizes TSC2 by inhibiting the interaction between TSC2 and the HERC1 ubiquitin ligase. *J. Biol. Chem.* **281:** 8313–8316

Clark GJ, Kinch MS, Rogers-Graham K, Sebti SM, Hamilton AD & Der CJ (1997) The Ras-related protein Rheb is farnesylated and antagonizes Ras signaling and transformation. *J Biol Chem* **272:** 10608–10615

Demetriades C, Plescher M & Teleman AA (2016) Lysosomal recruitment of TSC2 is a universal response to cellular stress. *Nat Commun* **7:** 10662

Dibble CC, Elis W, Menon S, Qin W, Klekota J, Asara JM, Finan PM, Kwiatkowski DJ, Murphy LO & Manning BD (2012) TBC1D7 is a third subunit of the TSC1-TSC2 complex upstream of mTORC1. *Mol Cell* **47:** 535–546

Gai Z, Chu W, Deng W, Li W, Li H, He A, Nellist M & Wu G (2016) Structure of the TBC1D7-TSC1 complex reveals that TBC1D7 stabilizes dimerization of the TSC1 C-terminal coiled coil region. *J Mol Cell Biol*

González A & Hall MN (2017) Nutrient sensing and TOR signaling in yeast and mammals. *EMBO J.* **36:** 397–408

Hansmann P, Brückner A, Kiontke S, Berkenfeld B, Seebohm G, Brouillard P, Vikkula M, Jansen FE, Nellist M, Oeckinghaus A & Kümmel D (2020) Structural analysis of the TSC2 GAP domain: mechanistic insight into catalysis and pathogenic mutations. *Structure*

Henske EP, Jóźwiak S, Kingswood JC, Sampson JR & Thiele EA (2016) Tuberous sclerosis complex. *Nat. Rev. Dis. Prim.* **2:** 16035

bioRxiv preprint doi: https://doi.org/10.1101/2020.09.29.319707; this version posted October 1, 2020. The copyright holder for this preprint (which was not certified by peer review) is the author/funder. All rights reserved. No reuse allowed without permission.

Hoogeveen-Westerveld M, Exalto C, Maat-Kievit A, van den Ouweland A, Halley D & Nellist M (2010) Analysis of TSC1 truncations defines regions involved in TSC1 stability, aggregation and interaction. *Biochim. Biophys. Acta - Mol. Basis Dis.* **1802:** 774–781

Huang J & Manning BD (2008) The TSC1-TSC2 complex: a molecular switchboard controlling cell growth. *Biochem J* **412:** 179–190

Menon S, Dibble CC, Talbott G, Hoxhaj G, Valvezan AJ, Takahashi H, Cantley LC & Manning BD (2014) Spatial control of the TSC complex integrates insulin and nutrient regulation of mTORC1 at the lysosome. *Cell* **156:** 771–785

Nellist M, van Slegtenhorst MA, Goedbloed M, van den Ouweland AM, Halley DJ & van der Sluijs P (1999) Characterization of the cytosolic tuberin-hamartin complex. Tuberin is a cytosolic chaperone for hamartin. *J Biol Chem* **274:** 35647–35652

Qin J, Wang Z, Hoogeveen-Westerveld M, Shen G, Gong W, Nellist M & Xu W (2016) Structural Basis of the Interaction between Tuberous Sclerosis Complex 1 (TSC1) and Tre2-Bub2-Cdc16 Domain Family Member 7 (TBC1D7). *J Biol Chem* **291:** 8591–8601

Ramlaul K & Aylett CHS (2018) Signal integration in the (m)TORC1 growth pathway. *Front. Biol. (Beijing).*: 1–26

Rohou A & Grigorieff N (2015) CTFFIND4: Fast and accurate defocus estimation from electron micrographs. *J. Struct. Biol.* **192:** 216–221

Santiago Lima AJ, Hoogeveen-Westerveld M, Nakashima A, Maat-Kievit A, Van Den Ouweland A, Halley D, Kikkawa U & Nellist M (2014) Identification of regions critical for the integrity of the TSC1-TSC2-TBC1D7 complex. *PLoS One* **9:**

Scheres SHW (2012) RELION: Implementation of a Bayesian approach to cryo-EM structure determination. *J. Struct. Biol.* **180:** 519–530

Scrima A, Thomas C, Deaconescu D & Wittinghofer A (2008) The Rap-RapGAP complex: GTP hydrolysis without catalytic glutamine and arginine residues. *EMBO J* **27:** 1145–1153

Shumway SD, Li Y & Xiong Y (2003) 14-3-3β binds to and negatively regulates the tuberous sclerosis complex 2 (TSC2) tumor suppressor gene product, tuberin. *J Biol Chem* **278:** 2089–2092

van Slegtenhorst M, Nellist M, Nagelkerken B, Cheadle J, Snell R, van den Ouweland A, Reuser A, Sampson J, Halley D & van der Sluijs P (1998) Interaction between hamartin and tuberin, the TSC1 and TSC2 gene products. *Hum Mol Genet* **7:** 1053–1057

Sun W, Zhu YJ, Wang Z, Zhong Q, Gao F, Lou J, Gong W & Xu W (2013) Crystal structure of the

bioRxiv preprint doi: https://doi.org/10.1101/2020.09.29.319707; this version posted October 1, 2020. The copyright holder for this preprint (which was not certified by peer review) is the author/funder. All rights reserved. No reuse allowed without permission.

yeast TSC1 core domain and implications for tuberous sclerosis pathological mutations. *Nat Commun* **4:** 2135

Tang G, Peng L, Baldwin PR, Mann DS, Jiang W, Rees I & Ludtke SJ (2007) EMAN2: An extensible image processing suite for electron microscopy. *J. Struct. Biol.* **157:** 38–46

Woodford MR, Sager RA, Marris E, Dunn DM, Blanden AR, Murphy RL, Rensing N, Shapiro O, Panaretou B, Prodromou C, Loh SN, Gutmann DH, Bourboulia D, Bratslavsky G, Wong M & Mollapour M (2017) Tumor suppressor Tsc1 is a new Hsp90 co‐chaperone that facilitates folding of kinase and non‐kinase clients. *EMBO J.* **36:** e201796700

Yang H, Jiang X, Li B, Yang HJ, Miller M, Yang A, Dhar A & Pavletich NP (2017) Mechanisms of mTORC1 activation by RHEB and inhibition by PRAS40. *Nature* **552:** 368–373

Zech R, Kiontke S, Mueller U, Oeckinghaus A & Kümmel D (2016) Structure of the Tuberous Sclerosis Complex 2 (TSC2) N Terminus Provides Insight into Complex Assembly and Tuberous Sclerosis Pathogenesis. *J Biol Chem* **291:** 20008–20020

Zheng SQ, Palovcak E, Armache JP, Verba KA, Cheng Y & Agard DA (2017) MotionCor2: Anisotropic correction of beam-induced motion for improved cryo-electron microscopy. *Nat. Methods* **14:** 331–332

Zivanov J, Nakane T, Forsberg B, Kimanius D, Hagen WJ, Lindahl E & Scheres SH (2018) RELION-3: new tools for automated high-resolution cryo-EM structure determination. *bioRxiv* **7:** 421123

bioRxiv preprint doi: https://doi.org/10.1101/2020.09.29.319707; this version posted October 1, 2020. The copyright holder for this preprint (which was not certified by peer review) is the author/funder. All rights reserved. No reuse allowed without permission.

Figure Legends

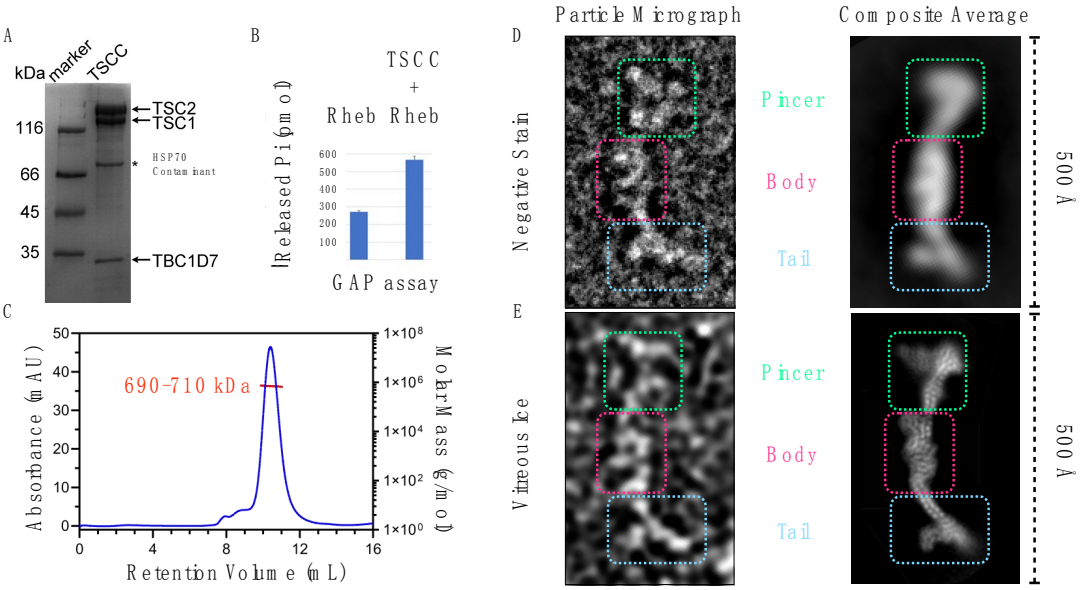

Figure 1: The human TSC protein complex is an elongated, flexible, scorpion-like complex with a defined "pincer", "body", and barbed "tail". [A] Coomassie-stained SDS-PAGE of purified holo-TSCC, demonstrating stoichiometric retrieval of all three components in good yield. [B] Results of three repetitions of a malachite green inorganic phosphate release assay conducted with purified Rheb and with purified Rheb and TSCC, showing a clear increase in activity in the presence of the TSCC. [C] SEC-MALLS trace and molecular weight estimate for TSC1$_{\Delta 400\text{-}600}$-TSC2-TBC1D7. The peak was isotropic, and the molecular weight estimate was well within range of the observed protein components upon later structural examination. [D] Electron micrograph of a negatively stained TSCC particle on a carbon support, and composite 2D average image of the TSCC from the windowed regions of negatively stained particles as indicated. [E] Electron micrograph of a TSCC particle frozen within vitreous ice on a graphene oxide support, and composite 2D average image of the TSCC from the windowed regions of vitrified particles as indicated. In each of panels D and E, the same regions, "pincer" (chartreuse), "body" (cerise), and "tail" (cerulean), are indicated through dashed boxes of the appropriate colour in both the representative particle image and the composite 2D class-average representation.

bioRxiv preprint doi: https://doi.org/10.1101/2020.09.29.319707; this version posted October 1, 2020. The copyright holder for this preprint (which was not certified by peer review) is the author/funder. All rights reserved. No reuse allowed without permission.

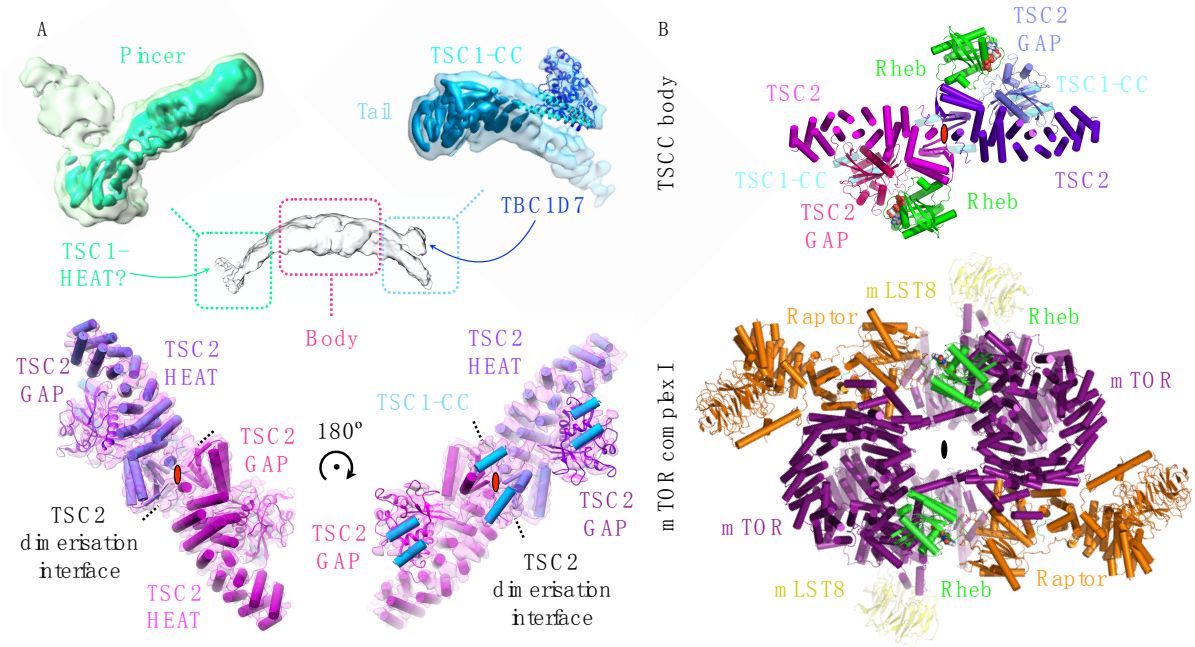

Figure 2: The TSCC exhibits C2 pseudo-symmetry which is broken by the interaction between TSC1 and TSC2, with the central TSC2 GAP domains poised to bind two Rheb molecules. [A] The overall structure of TSCC at low resolution (centre) and the refined densities corresponding to each region of the TSCC (indicated by boxes) are shown. In each case the reconstructed electron scattering density is shown as a transparent isosurface, while the corresponding fitted molecular structures, and secondary structural elements in the case of the body, are shown in cartoon representation where available and practicable. In the case of the "body" the reconstruction has been rotated by 180º in the second panel as indicated. [B] The docked fit of Rheb against the TSC2 GAP domain, based on the structure of the RapGAP-Rap1 complex, within the "body" of the TSCC, in comparison to its fit in the Rheb-activated structure of mTORC1. The secondary structural elements of the TSCC, and the molecular structure of mTORC1, are shown in cartoon representation.

bioRxiv preprint doi: https://doi.org/10.1101/2020.09.29.319707; this version posted October 1, 2020. The copyright holder for this preprint (which was not certified by peer review) is the author/funder. All rights reserved. No reuse allowed without permission.

Table 1: Frequent tumorigenic missense mutations of TSC2 in the Tuberous sclerosis database. Tumorigeic missense mutations of TSC2 with more than 5 entries in the Tuberous sclerosis database (http://chromium.lovd.nl/LOVD2/TSC/home.php?select_db=TSC2) are listed.

residue	Tumorigenic missense mutations of TSC2				Total entries
A84	A84V (5 entries)				5
P91	P91L (6 entries)				6
E92	E92V (8 entries)				8
C244	C244R (2 entries)	C244Y (3 entries)			5
M286	M286V (10 entries)	M286T (1 entry)			11
G294	G294R (1 entry)	G294E (2 entries)	G294V (2 entries)		5
E337	E337K (5 entries)				5
A357	A357V (5 entries)				5
R367	R367Q (17 entries)	R367P (1 entry)			18
G440	G440S (7 entries)				5
L448	L448P (4 entries)	L448R (1 entry)			5
A460	A460T (11 entries)				11
R462	R462G (2 entries)	R462C (1 entry)	R462H (6 entries)	R462P (2 entries)	11
L466	L466P (4 entries)	L466R (1 entry)			5
L493	L493V (4 entries)	L493P (2 entries)			6
A583	A583T (8 entries)				8
H597	H597Y (3 entries)	H597P (1 entry)	H597R (7 entries)	H597L (1 entry)	12
Y598	Y598H (5 entries)	Y598L (2 entries)			7
A607	A607T (7 entries)	A607S (1 entry)	A607E (1 entry)		9
R611	R611W (44 entries)	R611G (4 entries)	R611Q (87 entries)	R611P (1 entry)	136
R622	R622W (10 entries)	R622Q (1 entry)	R622P (4 entries)		15
M649	M649V (1 entry)	M649L (1 entry)	M649T (6 entries)		8
C696	C696R (4 entries)	C696Y (2 entries)			6
L826	L826M (8 entries)	L826P (3 entries)			11

L847	L847P (5 entries)	L847R (1 entry)				6
R905	R905W (49 entries)	R905G (2 entries)	R905Q (17 entries)			68
L916	L916P (3 entries)	L916R (2 entries)				5
R988	R988C (1 entry)	R988H (1 entry)	R988P (3 entries)			5
R1032	R1032P (8 entries)					8
R1044	R1044K (2 entries)	R1044T (1 entry)	R1044M (2 entries)			5
A1141	A1141T (1 entry)	A1141V (11 entries)				12
R1200	R1200W (28 entries)	R1200Q (1 entry)	R1200P (3 entries)			32
T1203	T1203P (4 entries)	T1203K (1 entry)				5
A1297	A1297T (8 entries)					8
P1305	P1305S (1 entry)	P1305L (5 entries)				6
R1329	R1329H (12 entries)					12
A1429	A1429S (10 entries)					10
P1497	P1497T (3 entries)	P1497S (2 entries)	P1497R (3 entries)	P1497L (4 entries)		12
D1535	D1535Y (2 entries)	D1535A (2 entries)	D1535V (1 entry)			5
Y1549	Y1549N (1 entry)	Y1549H (1 entry)	Y1549C (4 entries)			6
H1620	H1620Y (5 entries)	H1620R (1 entry)				6
G1642	G1642D (5 entries)					5
N1643	N1643H (3 entries)	N1643S (2 entries)	N1643I (1 entry)	N1643K (1 entry)		7
V1646	V1646M (3 entries)	V1646L (2 entries)	V1646G (1 entry)			5
Y1650	Y1650N (2 entries)	Y1650H (2 entries)	Y1650S (1 entry)	Y1650C (4 entries)		9
N1651	N1651H (2 entries)	N1651S (14 entries)				16
P1675	P1675L (55 entries)	P1675Q (2 entries)	P1675R (4 entries)			61
R1706	R1706C (3 entries)	R1706H (2 entries)				5
P1709	P1709L (12 entries)	P1709R (2 entries)				14
R1713	R1713H (9 entries)	R1713P (3 entries)				12
R1743	R1743G (2 entries)	R1743W (47 entries)	R1743Q (49 entries)	R1743P (6 entries)	R1743L (2 entries)	106
S1774	S1774T (9 entries)					9
G1787	G1787S (6 entries)					6
R1795	R1795C (7 entries)	R1795L (1 entry)				8